

A Mediator-Free Multi-Ply Biofuel Cell Using an Interfacial Assembly between Hydrophilic Enzymes and Hydrophobic Conductive Oxide Nanoparticles with Pointed Apexes

Minchul Kang, Donghyeon Nam, Jeongyeon Ahn, Yoon Jang Chung, Seung Woo Lee, Young-Bong Choi, Cheong Hoon Kwon,* and Jinhan Cho*

Biofuel cells (BFCs) based on enzymatic electrodes hold great promise as power sources for biomedical devices. However, their practical use is hindered by low electron transfer efficiency and poor operational stability of enzymatic electrodes. Here, a novel mediator-free multi-ply BFC that overcomes these limitations and exhibits both substantially high-power output and long-term operational stability is presented. The approach involves the utilization of interfacial interaction-induced assembly between hydrophilic glucose oxidase (GOx) and hydrophobic conductive indium tin oxide nanoparticles (ITO NPs) with distinctive shapes, along with a multi-ply electrode system. For the preparation of the anode, GOx and oleylamine-stabilized ITO NPs with bipod/tripod type are covalently assembled onto the host fiber electrode composed of multi-walled carbon nanotubes and gold (Au) NPs. Remarkably, despite the contrasting hydrophilic and hydrophobic properties, this interfacial assembly approach allows for the formation of nanoblended GOx/ITO NP film, enabling efficient electron transfer within the anode. Additionally, the cathode is prepared by sputtering Pt onto the host electrode. Furthermore, the multi-ply fiber electrode system exhibits unprecedented high-power output ($\approx 10.4 \text{ mW cm}^{-2}$) and excellent operational stability (2.1 mW cm^{-2} , $\approx 49\%$ after 60 days of continuous operation). The approach can provide a basis for the development of high-performance BFCs.

1. Introduction

Rapid advances in biomedical devices have created a strong demand for clean and sustainable power sources, which has led to the development of enzymatic biofuel cells (BFCs) that can convert biochemical energy into electricity efficiently under mild and normal physiological conditions (i.e., neutral pH and room temperature).^[1–5] Recently, the increasing versatility of implantable and miniaturized bioelectronics, such as pacemakers and cardioverter defibrillators, has further accelerated the demand for BFCs with higher power performance and longer operational stability.^[6–14] However, despite this need, their low power efficiency (a few to hundreds of $\mu\text{W cm}^{-2}$) and short lifespan (<8 days) have still remained critical issues, which have strongly restricted their widespread use in the biomedical industry.^[15–17] Particularly, the poor electron transfer efficiency and unfavorable interfacial interaction between enzymes and

M. Kang, D. Nam, J. Ahn, Y. J. Chung, J. Cho
Department of Chemical and Biological Engineering
Korea University
145 Anam-ro, Seongbuk-gu, Seoul 02841, Republic of Korea
E-mail: jinhan71@korea.ac.kr


S. W. Lee
The George W. Woodruff School of Mechanical Engineering Georgia
Institute of Technology
Atlanta, GA 30332, USA

Y.-B. Choi
Department of Chemistry
College of Science & Technology
Dankook University
Dandae-ro, Cheonan-si, Chungnam 31116, Republic of Korea

C. H. Kwon
Department of Energy Resources and Chemical Engineering
Kangwon National University
Samcheok 25913, Republic of Korea
E-mail: chkwon2@kangwon.ac.kr

J. Cho
KU-KIST Graduate School of Converging Science & Technology
Korea University
145 Anam-ro, Seongbuk-gu, Seoul 02841, Republic of Korea

J. Cho
Soft Hybrid Materials Research Center
Advanced Materials Research Division
Korea Institute of Science and Technology (KIST)
Seoul 02792, Republic of Korea

 The ORCID identification number(s) for the author(s) of this article can be found under <https://doi.org/10.1002/adma.202304986>

© 2023 The Authors. Advanced Materials published by Wiley-VCH GmbH. This is an open access article under the terms of the Creative Commons Attribution-NonCommercial License, which permits use, distribution and reproduction in any medium, provided the original work is properly cited and is not used for commercial purposes.

DOI: 10.1002/adma.202304986

the host electrode are the most important factors contributing to these drawbacks.

To address these challenges, various approaches have been developed to date, primarily focusing on improving electron transfer. One approach involves incorporating redox mediators with electrochemical activity into the enzymes.^[18–21] Generally, redox mediators can be electroreduced through the neighboring enzymes, and then diffuse to the surface of electrode, and subsequently transfer electrons from the active center (flavin adenine dinucleotide, FAD) of glucose oxidase (GOx) to the electrode.^[20–23] In this case, the long polymeric chains of redox mediator not only increase the apparent diffusivity of electrons but also facilitate electron transfer from the redox centers of GOx to the electrode. Owing to their effective electron transfer between electrodes and enzymes, the use of redox mediators in BFCs has led to substantial improvements in power output performance. Recently, several studies have reported mediator-based BFCs with considerably good power densities ranging from 1 to 2 mW cm⁻².^[16,24,25] However, using redox mediators can also bring about other issues, such as biological toxicity, complicated synthesis processes for the mediators, and a decrease (<0.8 V) in the open-circuit voltage (OCV).^[16,24,25] Generally, the mediators in mediator-based BFCs should maintain a stable redox state, become immobilized on the electrode with the enzyme, and undergo rapid and reversible redox reactions on the electrode's surface. To achieve these requirements, osmium-based mediators within polymer frameworks are commonly used.^[26] However, a significant challenge arises from the degradation of the polymer anchoring to the electrode, which leads to a loss in power density and ultimately causes a decline in BFC performance.^[27] Furthermore, the use of osmium complexes as mediators presents a potential cytotoxicity.^[28] Additionally, mediated electron transfer results in a lower open-circuit voltage compared to direct electron transfer due to the fixed potential inherent to this mechanism.

As an alternative, electrostatically charged conductive carbon-based nanomaterials, such as conductive multi-walled carbon nanotubes (MWCNTs), reduced graphene oxide (rGO), and nitrogen-doped carbon nitrides, which can be dispersed in aqueous media, have been used as electrode components to enhance the active surface area and facilitate electron transfer.^[29–31] Additionally, the incorporation of electrostatically charged metal nanoparticles (NPs) into enzymes has been explored to further enhance electron transfer capabilities.^[32–36] However, despite these significant efforts, achieving high power density above 1 mW cm⁻² in conductive nanomaterial-based BFCs without the use of redox mediators has proven challenging.^[30,35,37] This difficulty primarily stems from the low packing density and non-uniform assembly of electrostatically charged conductive components (by electrostatic repulsion in water), leading to inefficient electron transfer. Consequently, there is a pressing need to address these limitations and develop strategies to improve the performance of conductive nanomaterial-based BFCs.

Substantial research efforts have also been directed toward improving the long-term operational stability of BFCs through enzyme immobilization and orientation.^[36,38,39] Particularly, considering that the active center (FAD) of enzyme is buried ≈7–15 Å below the protein surface, enzyme immobilization also has an important effect on the electron transfer between enzyme and electrode as well as the operational stability.^[40] However, in the

case of immobilizing GOx on host electrode through traditional methods (mainly slurry casting) without any specific interfacial interaction, the thicknesses of physically adsorbed GOx films can be increased up to a few micrometers (μm), which is vulnerable to adhesion failure at the interfaces of GOx film/host electrode and interconnected GOx.^[41] Furthermore, in the case of using a 3D porous host electrode, it should be noted that these traditional methods have limited the formation of the conformal and robust GOx films, which have a significant effect on the operational stability of the resulting BFCs. Recently, robust immobilization of enzymes onto electrodes has been achieved through the use of polymeric linkers that can electrostatically or covalently bridge the interfaces between neighboring enzymes and/or between host electrode and enzyme.^[20,42–47] However, most BFCs using insulating polymeric linkers exhibited a considerably low power output with operational stability ranging from a few hours to 7 days (under continuous operation).^[16,48,49] As a result, there is a strong need for more novel approaches enabling robust interfacial interactions, unique conductive components, and optimized electrode design to develop BFCs with higher power output and longer operational stability.

Herein, we present a high-performance BFC that utilizes multi-ply fiber electrodes, employing an interfacial assembly between bipod- and/or tripod-type conductive oxide NPs in non-polar media and GOx in aqueous media. The key aspect of our approach lies in the covalent bonding-based interfacial assembly, which significantly enhances the electron transfer and operational stability of the GOx-based electrode by increasing the packing density and robust immobilization of hydrophobic conductive oxide NPs onto the GOx layer. This favorable interfacial interaction relies on a ligand exchange reaction facilitated by multiple affinities between the bare surface of oxide NPs and the amino acid groups within GOx, resulting in the replacement of loosely bound hydrophobic ligands by GOx during deposition. Additionally, it is important to note that hydrophobic conductive NPs without long-range electrostatic repulsion between the neighboring NPs can be densely assembled onto a hydrophilic GOx layer. This remarkable behavior enables the successful overcoming of the substantial difference in solvent polarity between nonpolar and aqueous media. Such adsorption behavior stands in stark contrast to that observed in traditional electrostatic interfacial assemblies, which often result in low NP packing density.^[50,51] We also highlight that highly conductive host electrodes can be prepared using small molecule linker-bridged Au NP-MWCNT nanocomposite assembly, which can effectively contribute to enhancing the electron transfer between the host electrode and GOx layer.

Furthermore, we have designed the conductive oxide NPs with a distinctive shape to optimize the electron transfer process. This shape enhances the probability of reaching the deep FAD center of GOx, thereby creating an efficient pathway for electron transfer between the electrode surface and the FAD center, as well as between neighboring FAD centers of GOx. The proximity of the FAD center and conductive oxide NPs, along with a sufficiently small energy barrier between them, has the potential to further enhance electron transfer, ultimately leading to improved BFC performance. Moreover, our study demonstrates the additional advantages of the multi-ply fiber structure in enhancing the areal power output. By increasing the active surface area without proportionally enlarging the electrode, this design significantly

enhances the BFC's performance. To the best of our knowledge, the utilization of hydrophobic conductive NPs characterized by pointed axes and multiple structures, along with a large active surface area, remains unexplored by other research groups.

For this study, carboxylic acid (COOH)-functionalized MWCNTs (i.e., COOH-MWCNTs) were first layer-by-layer (LbL) assembled with tris(2-aminoethyl)amine (TREN) onto cotton fibers composed of numerous hydroxyl (OH) group-functionalized cellulose fibrils using hydrogen-bonding interaction. The introduction of TREN linker, with extremely small molecular weight ($M_w \approx 146$), effectively reduced the contact resistance between neighboring COOH-MWCNTs, enabling the formation of robust COOH-MWCNT films. Subsequently, tetraoctylammonium bromide (TOABr)-stabilized Au NPs (TOABr-Au NPs) were LbL-assembled with TREN onto MWCNT multilayer-coated fibers for the preparation of conductive host electrode, resulting in an increased electrical conductivity of up to 9000 S cm^{-1} (including $15 \pm 1 \mu\text{m}$ thickness of cotton fibril) and a decreased resistivity of up to $1.1 \times 10^{-4} \Omega \text{ cm}$.

For the preparation of conductive oxide NPs with bipod/tripod shape and apexes, we synthesized oleylamine-stabilized indium tin oxide (OAm-ITO) NPs of $\approx 3\text{--}10 \text{ nm}$ in nonpolar media. These NPs were then LbL-assembled with GOx in aqueous media using multiple affinities between the surface of the ITO NP and the amino acid groups of GOx. These (OAm-ITO NP/GOx)_p multilayers were deposited onto the conductive fibers, forming an enzymatic anode that facilitated facile electron transfer within the GOx-based multilayers, all in a redox mediator-free system. Additionally, a Pt-sputtered conductive fiber was employed as the cathode of the BFC.

The resulting BFC composed of enzymatic anode fiber and Pt-sputtered fiber exhibited high areal power density, which could be further enhanced by plying the electrodes. With increasing the ply number of fiber electrodes from 1 to 3, the areal power density of BFCs (at 300 mmol L^{-1} glucose) was increased from ≈ 4.7 (showing the OCV of $\approx 1.0 \text{ V}$) to 10.4 mW cm^{-2} , outperforming the power density of BFCs reported to date. This level of power is not only sufficient to operate self-powered wireless sensors but also capable of powering a wide range of power-demanding biomedical devices such as drug pumps, cardiac pacemakers, and bone growth stimulators.^[52] Our multi-ply BFCs could maintain $\approx 49\%$ (corresponding to 2.1 mW cm^{-2}) of the initial power density at 10 mmol L^{-1} glucose even after 60 days, demonstrating their high operational stability. We believe that our approach can provide a basis for developing and designing high-performance BFCs with effective electron transfer and high operational stability.

2. Results and Discussion

2.1. Host Electrodes Using Au NP-MWCNT Multilayers

To prepare highly conductive fiber-based host electrodes, COOH-MWCNTs dispersed in ethanol were preferentially LbL-assembled with TREN molecules onto cotton fibers with a diameter of $\approx 220 \mu\text{m}$ using complementary hydrogen bonding interaction between COOH groups of MWCNTs and NH_2 groups of TREN molecules in ethanol (Figure 1a). It should be noted that TREN molecule, as a linker for connecting the neighboring

COOH-MWCNTs, was employed to enhance the electrical conductivity of MWCNT films. Owing to the use of extremely small TREN molecular linkers that directly bridged the interfaces between neighboring COOH-MWCNTs, the electrical contact resistance of the COOH-MWCNT-assembled multilayers can be significantly decreased compared to that of COOH-MWCNT multilayers bridged by other NH_2 -functionalized polymeric linkers such as poly(ethylene imine) (PEI) or poly(allylamine hydrochloride) (PAH) (the more details are given later).

The adsorption behavior of LbL-assembled (COOH-MWCNT/TREN)_n films was qualitatively and quantitatively investigated by UV-vis spectroscopy and quartz crystal microbalance (QCM), respectively. As shown in Figure 1b and Figure S1, Supporting Information, the UV-vis absorbance of multilayers was almost linearly increased with increasing the bilayer number (*n*), indicating the vertical growth of the regular multilayer film. Figure 1c shows the frequency changes, $-\Delta F$, and the mass changes (Δm) in the adsorbed COOH-MWCNTs and TREN resulting from an increase of bilayer number (*n*) (see Experimental Section, Supporting Information). The mass changes were calculated from the frequency changes of the COOH-MWCNTs and TREN layers adsorbed on the crystal surface. In this case, the loading amounts per COOH-MWCNT/TREN bilayer were calculated to be $\approx 1.4 \pm 0.1 \mu\text{g cm}^{-2}$. Using this LbL-assembled behavior, the (COOH-MWCNT/TREN)_n multilayers were deposited onto the $15 \pm 1 \mu\text{m}$ -thick cotton fibrils (within $\approx 220 \mu\text{m}$ -thick cotton fiber). In this case, the electrical properties of the formed fibers were gradually enhanced by increasing the bilayer number (*n*). Specifically, the electrical conductivity and resistivity of (COOH-MWCNT/TREN)₁₀ multilayer-coated fibers (shortly 10-MWCNT/fiber) were measured to be $\approx 0.1 \text{ S cm}^{-1}$ and $8.9 \Omega \text{ cm}$, respectively (Figure 1d). In addition, the 10-MWCNT/fibers maintained their highly uniform fibril structure without significant agglomeration (Figure 1e).

Another important advantage of this approach is that the COOH-MWCNT/TREN multilayer forest formed onto cotton fiber can induce the stable and robust adsorption of additional conductive metal NPs due to the high affinity (i.e., covalent-bonding) between Au NPs and primary amine (NH_2) groups of the outermost TREN layer. Spherical-type TOABr-Au NP with a diameter of $\approx 8 \text{ nm}$ in toluene could be LbL-assembled with TREN in ethanol via consecutive ligand exchange reaction between bulky TOABr ligands and TREN molecules, which was confirmed by UV-vis spectroscopy, Fourier transform infrared (FTIR) spectroscopy, and field-emission scanning electron microscopy (FE-SEM) (Figure 1f,g and Figures S2–S5, Supporting Information). In this case, it should be noted that the Au NP layers buried within the (TOABr-Au NP/TREN)_n multilayers had few bulky TOABr ligands, and only one TREN molecule layer directly and robustly bridged all interfaces between the vertically adjacent Au NP layers and between the abovementioned COOH-MWCNT layers as well as between cotton fibrils and COOH-MWCNTs. As a result, the electrical conductivity of the (TOABr-Au NP/TREN)₂₀/(COOH-MWCNT/TREN)₁₀-coated fiber (i.e., 20-Au-MWCNT/fiber) increased up to $\approx 9000 \text{ S cm}^{-1}$ without additional chemical and/or thermal treatments, surpassing those of the (TOABr-Au NP/TREN)₂₀-coated fiber without MWCNT multilayers (i.e., 20-Au/fiber) and 10-MWCNT/fiber without Au NPs. (Figure 2a and Figure S6, Supporting Information).

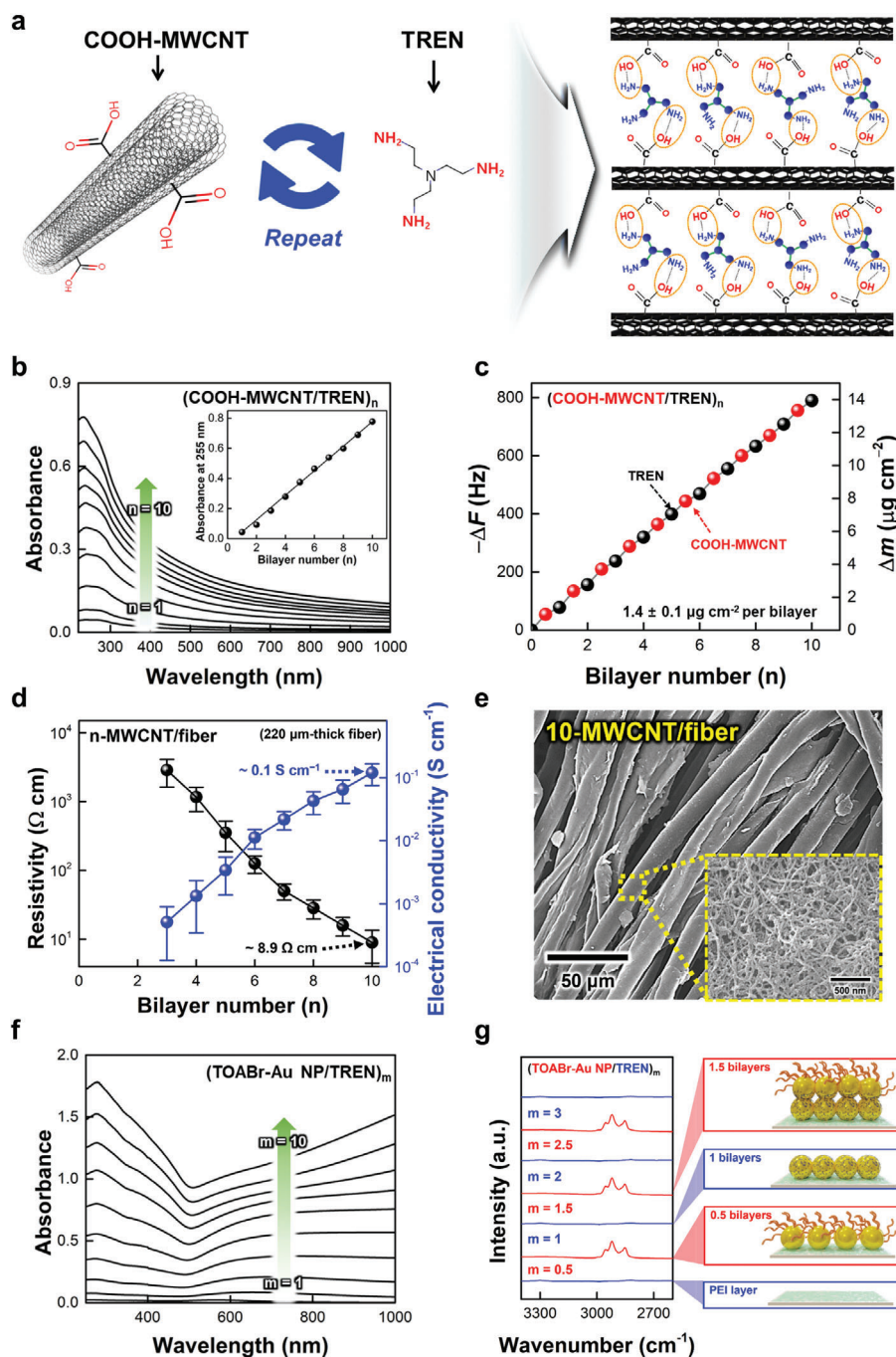


Figure 1. Characterization of $(\text{COOH-MWCNT/TREN})_n$ and $(\text{TOABr-Au NP/TREN})_m$ multilayers. a) The molecular and multilayer structures of COOH-MWCNT and TREN. b) UV-vis absorbance spectra of $(\text{COOH-MWCNT/TREN})_n$ with increasing bilayer number (n) from 1 to 10 and the hyperchromicity at 255 nm (inset). c) Frequency ($-\Delta F$) and mass change (Δm) of $(\text{COOH-MWCNT/TREN})_n$ multilayers by using QCM with increasing bilayer number (n) from 0 to 10. d) Resistivity and electrical conductivity of $(\text{COOH-MWCNT/TREN})_n$ multilayers as a function of bilayer number (n). e) FE-SEM image of $(\text{COOH-MWCNT/TREN})_{10}/\text{fiber}$. f) UV-vis absorbance spectra of the $(\text{TOABr-Au NP/TREN})_m$ multilayers with increasing bilayer number (m) from 1 to 10. g) FTIR spectra and schematic illustration of the $(\text{TOABr-Au NP/TREN})_m$ multilayers.

Additionally, the 20-Au-MWCNT/fiber exhibited evident gold color (by the naked eye) (Figure 2b); nevertheless, the 20-Au-MWCNT/fiber maintained the porous fibril structure of pristine cotton fibers without significant Au NP aggregation FE-SEM and energy-dispersive X-ray spectroscopy (EDS) images (Figure 2c).

Based on these results, the electrochemical properties of Au-MWCNT/fiber were examined as a function of bilayer number (m) at a scan rate of 5 mV s^{-1} . A three-electrode cell configuration was used in a 20 mmol L^{-1} phosphate-buffered saline (PBS) solution containing 300 mmol L^{-1} glucose under ambient

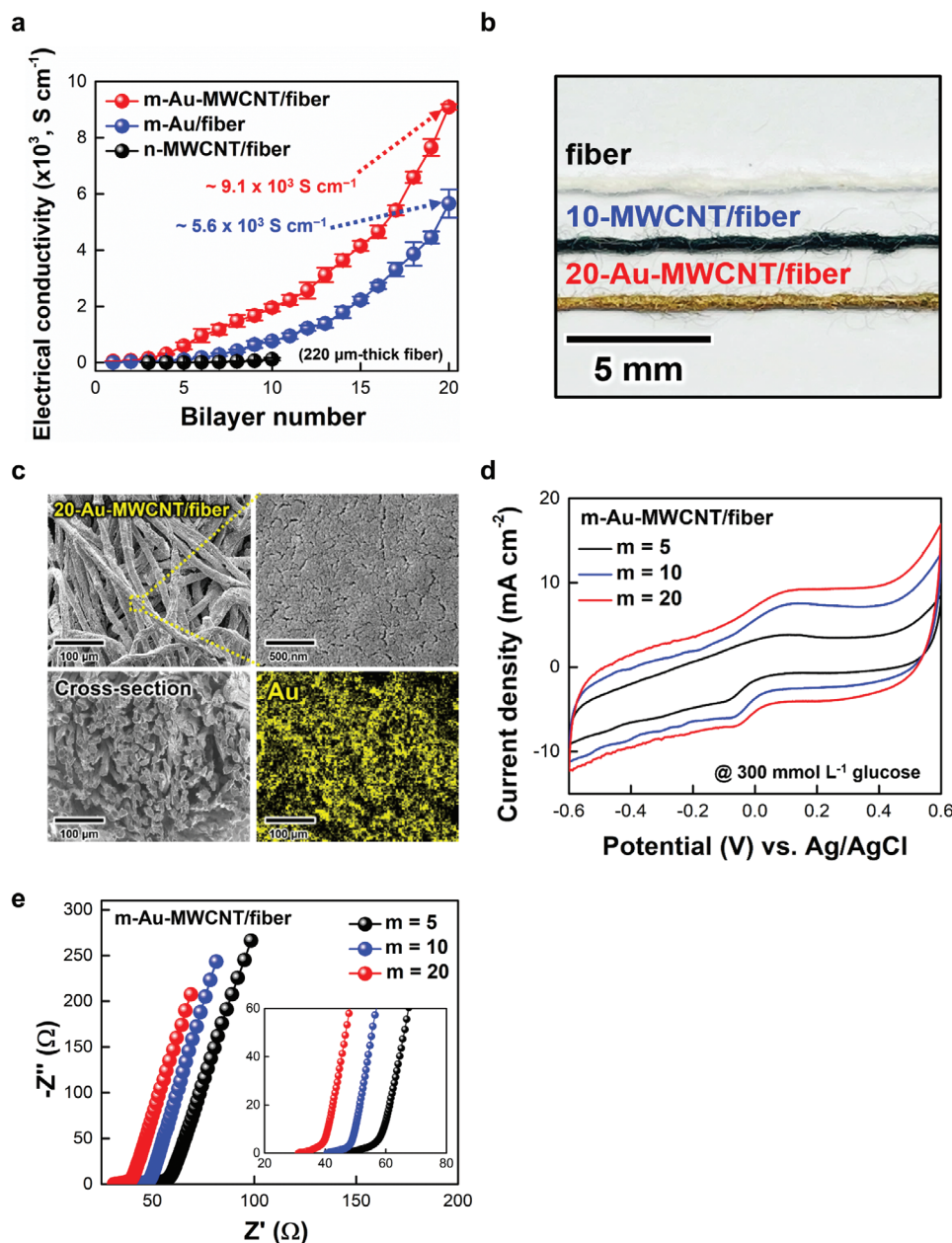


Figure 2. Surface morphology and electrochemical performance of host electrode. a) Electrical conductivity of m-Au-MWCNT/fiber, m-Au/fiber, and n-MWCNT/fiber as a function of (m) and (n). b) Photographic images of bare fiber (top), 10-MWCNT/fiber (middle), and 20-Au-MWCNT/fiber (bottom). c) Planar, cross-sectional FE-SEM, and energy-dispersive X-ray spectroscopy (EDS) mapping images of the 20-Au-MWCNT/fiber. d) CV curves of m-Au-MWCNT/fiber ($m = 5, 10, \text{ and } 20$) at a scan rate of 5 mV s^{-1} in a phosphate-buffered saline (PBS) solution containing 300 mmol L^{-1} glucose at $36.5 \text{ }^\circ\text{C}$. e) Nyquist plots of m-Au-MWCNT/fiber ($m = 5, 10, \text{ and } 20$) in PBS solution containing 300 mmol L^{-1} glucose at $36.5 \text{ }^\circ\text{C}$ and magnification in the high frequency range (inset).

conditions (Figure 2d). With increasing the bilayer number (m) of m-Au-MWCNT/fiber from 5 to 20, the cyclic voltammetry (CV) curves exhibited a gradual increase in cathodic and anodic current densities, which also displayed higher current density than 20-Au/fiber and 10-MWCNT/fiber (Figure S7, Supporting Information). These phenomena were mainly due to the increased electrical conductivity and active surface area of Au NP-coated fibers. Particularly, the results obtained from electrochemical impedance spectroscopy (EIS) evidently demonstrated that the

enhanced electrical conductivity of m-Au-MWCNT/fiber significantly decreased equivalent series resistance (ESR) and charge transfer resistance (R_{ct}) (Figure 2e). That is, with increasing the bilayer number (m) from 5 to 20, their ESR and R_{ct} decreased from 49 and 11 to 33 and $8 \text{ } \Omega$ (at 1 kHz), respectively. However, the m-Au-MWCNT/fiber exhibited similar linear slopes (i.e., Warburg slope) in the low-frequency region, indicating that the ion transport kinetics were almost constantly preserved. The resulting 20-Au-MWCNT/fiber, as a host electrode, possessed a

highly uniform surface morphology, large surface area, high electrical conductivity, and adjustable electrochemical properties.

2.2. Fiber-Based Anodes Using ITO NP-Incorporated GOx Multilayers

To alleviate the poor electron transfer between neighboring GOx and between the electrode and GOx that causes the low power output of enzyme-based BFCs, conductive oxide NPs were nanoblended with GOx using an unconventional LbL assembly onto the conductive fibers (CF) based on 20-Au-MWCNT/fibers. To achieve this goal, we first synthesized toluene-dispersible OAm-ITO NPs with bipod or tripod shapes instead of spherical-type metal NPs for the LbL assembly with GOx in aqueous solution (Figure 3a and Figure S8, Supporting Information). The size of OAm-ITO NPs ranged from 4–10 nm for the minor axis of ITO NPs to 8–16 nm for the major axis. Additionally, the NH₂ and COOH moieties of amino acid groups had a high affinity for the bare surface of ITO NPs. Therefore, bulky OAm ligands bound to the surface of ITO NPs could be replaced by GOx during LbL assembly, which could directly bridge the interfaces between vertically adjacent conductive ITO NPs (Figure 3b and Figure S9, Supporting Information). Although this replacement cannot be easily analyzed by FTIR due to the various chemical moieties of GOx, we could indirectly confirm the ligand exchange reaction between GOx and OAm-ITO NPs through the use of COOH-functionalized linkers (poly(acrylic acid) (PAA) or tricarballic acid (TC)) and NH₂-functionalized linkers (PEI or TREN). Specifically, two different multilayers, (OAm-ITO NP/PAA or TC)_p and (OAm-ITO NP/PEI or TREN)_p multilayers, exhibited a regular increase in UV–vis absorbance with increasing bilayer number (*p*), implying the formation of high multiple affinity between COOH and ITO NPs as well as between NH₂ and ITO NPs (Figures S10 and S11, Supporting Information).

It is important to note that the nonpolar toluene solvent used for the adsorption of OAm-ITO NPs onto the GOx-coated substrate could not infiltrate the hydrophilic GOx layer due to the hydration layer formed on the GOx layer. To confirm this possibility, the surface wettability throughout the alternating deposition of hydrophilic GOx and hydrophobic OAm-ITO NPs was first investigated by measuring the water contact angle of (OAm-ITO NP/GOx)_p multilayer film. When the GOx was initially coated onto an Au-sputtered Si-wafer, the water contact angle was measured to be ≈40°. However, subsequent deposition of OAm-ITO NPs decreased the water contact angle to ≈100°. These water contact angles periodically fluctuated as a result of the ligand exchange reaction when the outermost layer was changed from GOx to OAm-ITO NP and vice versa (Figure S12, Supporting Information). Based on these results, it is reasonable to conjecture that the GOx layers buried within (OAm-ITO NP/GOx)_p multilayers could be biologically active even in nonpolar media such as toluene. The FTIR absorption bands of (OAm-ITO NP/GOx)_p multilayers almost coincided with those of the pristine GOx layer, providing concrete evidence to demonstrate such a possibility. In particular, given that the FTIR absorption bands of biologically active GOx exhibited the typical amide I (1650 cm⁻¹) and amide II (at 1539 cm⁻¹) absorption bands, these results clearly implied that the immobilized GOx layers within the (OAm-ITO

NP/GOx)_p multilayers still maintained an active conformation (Figure 3b and Figure S13, Supporting Information). That is, considering that the toluene solvent was used for the deposition of OAm-ITO NPs onto the immobilized GOx layer, these results indicated that toluene solvent had no effect on the bioactivity and conformational change of immobilized GOx layer. On the other hand, in the case of ethanol- and heat-treated GOx-based anodes (i.e., denatured p-anodes), we could not confirm any corresponding electrocatalytic signals originating from active GOx layers (i.e., ethanol-treated and heat-treated p-anodes) (Figure S14, Supporting Information).

As expected, the UV–vis absorbance of (OAm-ITO NP/GOx)_p multilayers increased linearly with increasing bilayer number (*p*) (Figure 3c and Figure S15, Supporting Information). The loading amount per bilayer obtained from QCM measurement was estimated to be ≈4.9 ± 0.2 μg cm⁻² (Figure 3d). In this case, the total film thickness of the (OAm-ITO NP/GOx)_p multilayers with a uniform and smooth surface morphology increased from 11 to 54 nm with increasing bilayer number (*p*) from 1 to 9, resulting in one bilayer thickness of ≈5.6 nm (Figure 3e). Since one bilayer thickness was smaller than the average size (≈8 nm) of OAm-ITO NPs, this phenomenon implied that the surface coverage of ITO NPs per layer was insufficient in the lateral dimension. As a result, the internal structure of (OAm-ITO NP/GOx)_p multilayers possessed a mixed and nanoblended structure instead of a stratified layer structure. This nanoblended structure could be indirectly confirmed by EDS mapping images (Figure 3f and Figure S16, Supporting Information). Additionally, these results suggested the possibility that electron transfer between neighboring GOx layers could be enhanced through the perfect nano-convergence of GOx and conductive ITO NP layers despite the extremely different surface polarities existing between hydrophilic GOx in water and hydrophobic OAm-ITO NPs in toluene. Furthermore, we highlight that this nanoblending assembly using OAm-ITO NPs can also be achieved with other biomaterials such as ferritin, catalase, and hemoglobin-containing amino acid groups (Figure S17, Supporting Information).

Based on these results, we investigated the electrochemical properties of enzymatic electrodes (i.e., anode) that contained a multilayer thin film, (OAm-ITO NP/GOx)_p, on the CF electrode (Figure 4a). The (OAm-ITO NP/GOx)_p multilayers were deposited onto the CF (i.e., 20-Au-MWCNT/fiber) to prepare BFC anodes and investigate their glucose oxidation abilities in pH 7.4 PBS solution (Figure 4b). With an increasing bilayer number (*p*) of (OAm-ITO NP/GOx)_p multilayer-coated electrode (shortly p-anode) from 1 to 7, the maximum anodic current density of p-anode measured at +0.6 V gradually increased from 16.9 to 28.7 mA cm⁻², then decreased to 24.4 mA cm⁻² (in this case, the normalized anodic current densities at +0.6 V increased from 2.1 to 11.8, and then decreased to 7.5 mA cm⁻²), mainly due to the trade-off between the increased mass loading of GOx and the reduced electric field (by the increase of the total film thickness) (Figure 4c and Figure S18, Supporting Information). Therefore, in the case of p-anode, the optimized bilayer number (*p*) for a high-performance anode was determined to be *p* = 5, and its maximum anodic current density was estimated to be ≈28.7 mA cm⁻² at a glucose concentration of 300 mmol L⁻¹.

Based on the high anodic current density obtained from the 5-anode, we investigated its electrochemical performance as a func-

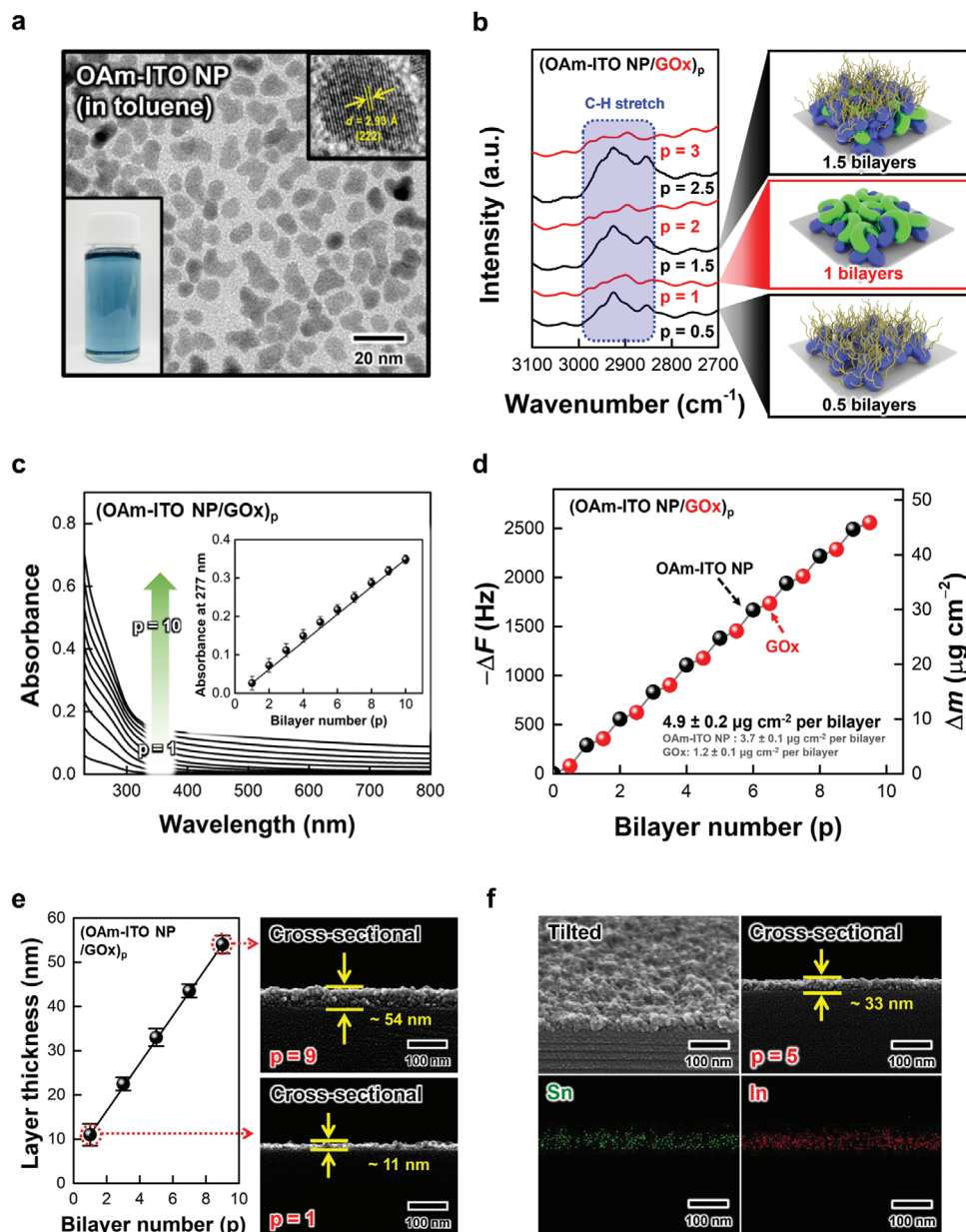


Figure 3. Deposition mechanism analysis of the $(\text{OAm-ITO NP}/\text{GOx})_p$ multilayers. a) HR-TEM images of OAm-ITO NPs with a lattice fringe spacing (d) of 2.93 Å corresponding to the (311) phase. Inset is a photographic image of OAm-ITO NP solution (in toluene). b) FTIR spectra and schematic illustration of the $(\text{OAm-ITO NP}/\text{GOx})_p$ multilayers as a function of bilayer number (p). c) UV-vis spectra of the $(\text{OAm-ITO NP}/\text{GOx})_p$ multilayers with increasing bilayer number (p) from 1 to 10 and the hyperchromicity at 277 nm (inset). d) Frequency ($-\Delta F$) and mass change (Δm) of $(\text{OAm-ITO NP}/\text{GOx})_p$ multilayers onto quartz substrate as a function of periodic number (p). e) Thickness of $(\text{OAm-ITO NP}/\text{GOx})_p$ multilayer film as a function of bilayer number (p) (left) and cross-sectional FE-SEM image of $(\text{OAm-ITO NP}/\text{GOx})_p$ multilayer ($p = 1$ and 9) (right). f) Cross-sectional FE-SEM and EDS mapping images of the $(\text{OAm-ITO NP}/\text{GOx})_5$ multilayer.

tion of glucose concentration. Increasing the glucose concentration from 0 to 300 mmol L⁻¹ resulted in a notable increase in the maximum anodic current density from 10.0 to 28.7 mA cm⁻² (Figure 4d). Additionally, the normalized anodic current density, obtained after eliminating the maximum anodic current density at a glucose concentration of 0 mmol L⁻¹, increased from 3.2 to 18.7 mA cm⁻². Furthermore, we conducted an investigation into the charge contribution of the 5-anode using Dunn's

method to validate the Faradaic current derived from the CV curves.^[53] Notably, as the glucose concentration was raised from 10 to 300 mmol L⁻¹, we observed a corresponding increase in the Faradaic charge, from 1.02 to 2.17 C cm⁻². These results establish a clear and direct correlation between the glucose concentration and the Faradaic charge of the 5-anode generated from the electrooxidation process by GOx (Figures S19 and S20, Supporting Information). As the concentration of glucose increased, a

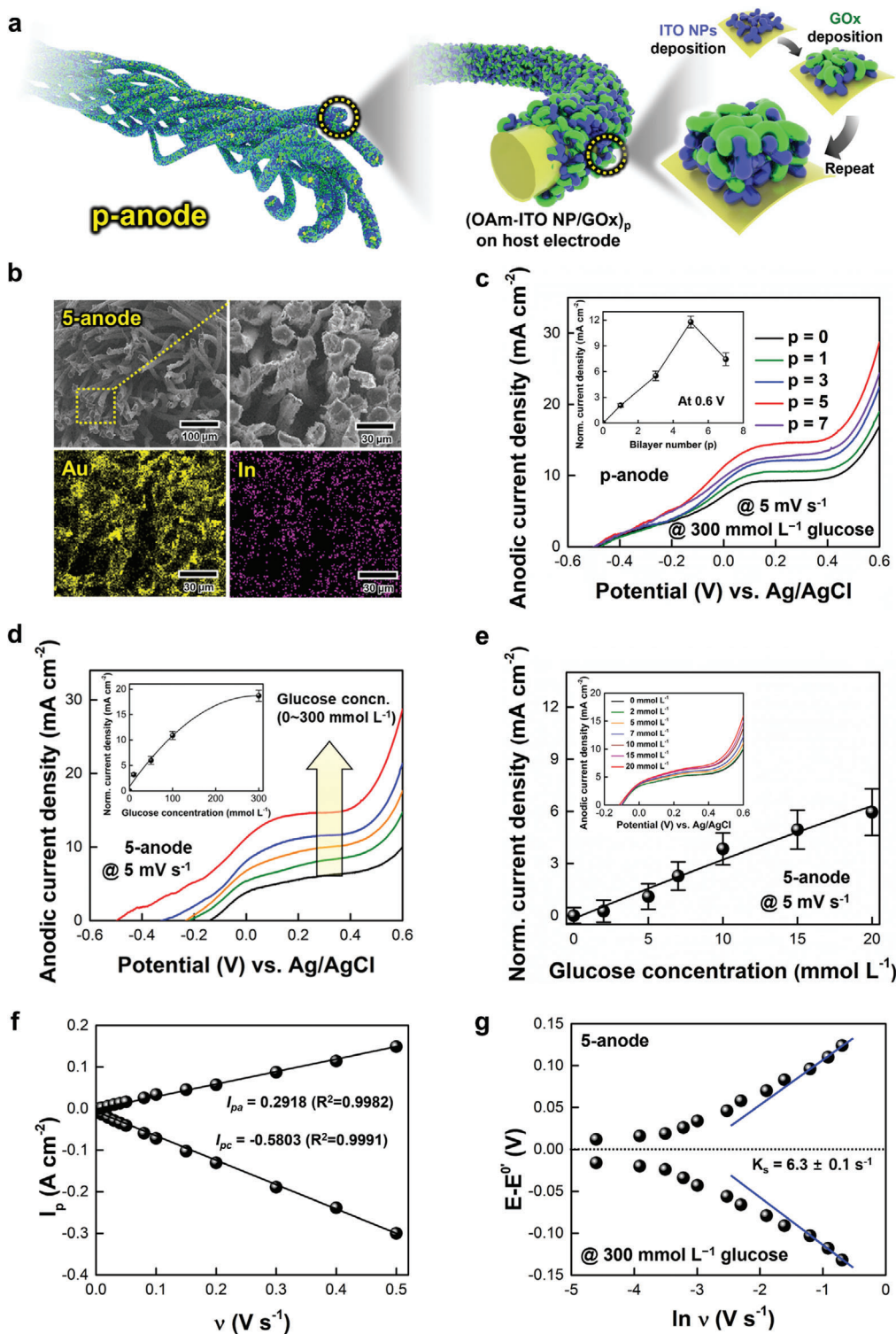


Figure 4. Electrochemical performance of p-anode. a) Schematic illustration of p-anode. b) Cross-sectional FE-SEM and EDS mapping images of the 5-anode. c) Anodic current density curves of the p-anode as a function of bilayer number (p) and the normalized anodic current density levels at +0.6 V (inset). d) Anodic current density curves of 5-anode with increasing concentration of glucose from 0 to 300 mmol L⁻¹ at 36.5 °C (the glucose concentrations of 0, 10, 50, 100, and 300 mmol L⁻¹ are ordered from bottom to top of the curve, respectively). The normalized anodic current density levels at +0.6 V are depicted in the inset. e) Normalized anodic current density levels of 5-anode at low glucose concentration from 0 to 20 mmol L⁻¹ at 36.5 °C. The anodic current densities of 5-anode with increasing glucose concentration from 0 to 20 mmol L⁻¹ at 36.5 °C are depicted in inset. f) Change in the peak current of the 5-anode with increasing the scan rate (ν) from 0.005 to 0.5 V s⁻¹ in PBS solution containing 300 mmol L⁻¹ glucose at 36.5 °C. g) Change in the potential ($E-E^0$) of 5-anode as a function of $\ln \nu$ at a 300 mmol L⁻¹ glucose.

slight rise in cathodic current was observed below -0.1 V during the negative potential scan of the 5-anode. This increase in current is primarily attributed to the adsorption of hydrogen ions (H^+) or other charged intermediates that are produced during the oxidation process of glucose.^[54,55] It is assumed that the higher glucose concentration promoted the oxidation reaction of glucose, leading to the generation of more hydrogen ions, which, in turn, resulted in increased adsorption of hydrogen ions onto the electrode, increasing the cathodic current. Moreover, the adsorption of hydrogen ions (H^+) can cause the reduction reaction of FAD-moieties of GOx, it can contribute to an increase in the cathodic current density by increasing the glucose concentration.^[56] Furthermore, the observed linear dependence of the normalized current densities on the low glucose concentration range of 5 to 20 mmol L⁻¹, which corresponds to the physiological condition, indicates that the 5-anode has potential for use in various glucose biosensors including diabetes sensors for continuous glucose monitoring systems (Figure 4e).

The electron transfer kinetics of the 5-anode were also investigated using the Laviron model.^[57] The anodic and cathodic peak currents of the 5-anode linearly increased with increasing the scan rate (Figure 4f) and followed Equation 1:

$$I_p = \frac{nFQ\nu}{4RT} \quad (1)$$

where I_p , n , Q , and ν are the peak current density, the number of electrons transferred ($n = 2$), the total charge adsorbed on the electrode, and the scan rate, respectively. F , R , and T are Faraday's constant, gas constant coefficient, and temperature.

This result indicates that the charge transfer reaction of the 5-anode is quasi-reversible and surface-controlled, providing a constant charge value independent of scan rates. Additionally, we experimentally determined the apparent heterogeneous electron transfer rate constant (K_s) using Equations 2 and 3, with a calculated value of 6.3 ± 0.1 s⁻¹ for the 5-anode, much higher than those (1.5 – 3.3 s⁻¹) previously reported for BFC anodes (Figure 4g and Figure S21, Supporting Information)^[30,58–60]:

$$E = E^{0'} + \frac{RT}{\alpha nF} \ln \frac{RTK_s}{\alpha nF} - \frac{RT}{\alpha nF} \ln \nu \quad (2)$$

$$E = E^{0'} + \frac{RT}{(1-\alpha)nF} \ln \frac{(1-\alpha)nF}{RTK_s} + \frac{RT}{(1-\alpha)nF} \ln \nu \quad (3)$$

where α is the electron transfer coefficient.

This high K_s value suggests that the GOx-immobilized electrode has a fast and efficient heterogeneous electron transfer process, mainly due to the redox reaction between the buried redox center of GOx (FAD center) and the surface of the host electrode (Equation 4)^[61]:



To further confirm the contribution of ITO NPs to the improvement of electron transfer kinetics in the GOx layer, we compared the rate constants of the GOx layer and the (ITO NP/GOx)₁ layer (Figure S22, Supporting Information), finding

the rate constant of the (ITO NP/GOx)₁ layer to be approximately two times higher than that of the ITO NP-free GOx layer. This difference is mainly attributed to the conductive ITO NPs' structural uniqueness, which effectively reduces the electron tunneling distance between the FAD center of GOx and the host electrode.

We also evaluated the ESR values and Warburg slopes of the 5-anode as a function of glucose concentration using EIS. As shown in Figure S23, Supporting Information, ESR values increased from 25.8 to 47.1 Ω at 1 kHz as glucose concentration increased from 0 to 300 mmol L⁻¹, while Warburg slopes were slightly decreased. These results implied that electron transfer was facilitated within the OAm-ITO NP/GOx multilayer-based anode. Furthermore, we investigated the relative change (RC) capacitance ($\Delta C/C_0$), a commonly used parameter for determining enzyme immobilization on the electrode surface obtained from the constant phase element (CPE) value of EIS. The RC capacitance value is calculated by dividing the change in capacitance (ΔC) measured at different glucose concentrations by the initial capacitance (C_0), which represents the non-faradaic reactions of the electrode surface, particularly the reactions of the ITO NPs and host electrode (specifically, Au NPs and MWCNTs) (Figure S24, Supporting Information).^[62] The resulting linear increase of the RC capacitance was mainly caused by GOx immobilized on the electrode surface. Therefore, this finding confirms that glucose directly reacts with the electrode surface, demonstrating the successful operation of the electron transfer through GOx in the absence of a redox mediator.

As a result, the use of ITO NP-incorporated GOx multilayers in our approach could induce close contact between GOx and conductive ITO NPs, as well as nanoblended OAm-ITO NP/GOx nanocomposites, which generated a strong electron relay effect within the overall film and lowered the contact resistance between vertically adjacent GOx layers. These unique characteristics of p-anodes were in stark contrast to those of conventional GOx-based electrodes produced by the cross-linking method, as well as the organic linker-based multilayer (i.e., (PEI/GOx)_n or (TREN/GOx)_n) anode that was LbL-assembled without the inclusion of conductive ITO NPs (Figures S25–S27, Supporting Information).^[63,64] In particular, the electrochemical behavior of the 5-anode, which was composed of (OAm-ITO NP/GOx)₅/CF, was characterized by its frequency dependence. This characteristic could be further characterized by the knee frequency, which is defined as the crossover point from the charge transfer reaction to the diffusion-controlled region. In this case, the 5-anode exhibited a higher knee frequency compared to conventional GOx-based anodes and (PEI or TREN/GOx)₅-based anodes. These results evidently indicated that the 5-anode could have more facile charge transfer and better mass transport during electrochemical operations due to the incorporated ITO NPs and the highly porous structure of the overall electrode (refer to Figure S26d, Supporting Information). As a result, the 5-anode retained 94.2% of its initial current density after continuous operation for 2 hr, proving the excellent operation stability (Figure S28, Supporting Information). Additionally, the residual toluene in the (OAm-ITO NP/GOx)₅/CF anode was not detected (Figure S29, Supporting Information), thereby ensuring its biological non-toxicity.

2.3. Pt-Sputtered Fiber Cathode

Based on anodes with effective electron transfer, we attempted to prepare a high-performance cathode. Firstly, we improved the oxygen reduction reaction (ORR) activity of the cathode by additionally sputtering Pt with excellent ORR activity onto the outermost TREN layer-coated host electrode (i.e., CF or 20-Au-MWCNT/fiber) via a vacuum sputtering process. In this case, Pt was sputtered onto both sides of CF. Cross-sectional FE-SEM and EDS mapping images (Figure S30, Supporting Information) revealed a uniform distribution of sputtered Pt (sputtering time ≈ 90 s) and Au NP over the entire area of CF. Increasing the Pt sputtering time from 0 to 90 s resulted in the current densities of the formed Pt-sputtered CFs (i.e., Pt/CFs) cathodes increasing from -12.3 to -25.8 mA cm $^{-2}$ (at a potential of -0.6 V) under ambient conditions (Figure S31, Supporting Information). In particular, it was confirmed that, with the introduction of Pt sputtering, the reduction reaction began to directly improve from $+0.54$ V, which is the open circuit potential of our cathode. The degree of the reduction reaction increased overall in the entire voltage range. This means that not only is the current generation improved in the entire voltage range, but also, when combined with an anode, it can directly contribute to an increase in power in a wide OCV range.

We also investigated the charge transfer effect of the Pt/CF cathode using EIS obtained from the fitting of Randle's equivalent circuit. To this end, the ESR values of Pt/CF electrodes with different Pt sputtering times (i.e., 0, 30, 60, and 90 s) were measured at a scan rate of 5 mV s $^{-1}$ using a three-electrode cell configuration in PBS solution. With increasing Pt sputtering time, the ESR values of Pt/CFs decreased from 25.8 to 19.8 Ω (Figure S32, Supporting Information). To obtain more detailed information about the frequency-dependent electrochemical behavior of Pt/CFs, the knee frequencies, which are defined as a crossover point from the charge transfer reaction to the diffusion-controlled region, were also obtained from the admittance plots (Figure S33, Supporting Information). In this case, the knee frequency (≈ 90 Hz) of the Pt/CFs prepared from the Pt sputtering time of 90 s (i.e., 90 s-Pt/CF) was higher than those of the Pt/CFs with different Pt sputtering times (specifically knee frequency ≈ 24 Hz for 0 s, ≈ 46 Hz for 30 s, and ≈ 76 Hz for 60 s), implying that 90 s-Pt/CF enabled more facile mass transport during electrochemical operations.

Based on these results, the ORR activities of the 90 s-Pt/CFs were measured under three different conditions (nitrogen (N $_2$)-, air-, and oxygen (O $_2$)-saturated PBS solutions). In this case, the cathodic current densities of 90 s-Pt/CFs (at a potential of -0.6 V) under N $_2$ -, air-, and O $_2$ -saturated conditions were ≈ -7.5 , -22.6 and -30.8 mA cm $^{-2}$, respectively (Figure S34, Supporting Information). Additionally, the normalized areal current density levels were obtained by subtracting the cathodic current density level measured at a specific potential of -0.6 V in an O $_2$ -free condition (i.e., N $_2$ -saturated condition) from the cathodic current density level measured at the same potential in air or O $_2$ -rich condition. Based on the -7.5 mA cm $^{-2}$ in the oxygen-free N $_2$ condition, the normalized areal cathodic current densities at -0.6 V were -15.1 mA cm $^{-2}$ under the air condition, and -23.3 mA cm $^{-2}$ under the O $_2$ -saturated condition, respectively. Considering that the cathodic current density level of a nonporous bulk Au wire

with the same diameter in the air condition was estimated to be ≈ -1.0 cm $^{-2}$ (Figure S35, Supporting Information), the cathodic behavior of 90 s-Pt/CF was considerably remarkable. This was mainly due to its extremely large active surface area of fibril-structured host electrode, as well as the conformal coating of highly active Pt onto all fibrils.

2.4. Power Generation of Full Cell Devices Using Multi-Ply BFC Electrodes

Based on these results, we prepared the fiber-based complete BFC composed of anode (i.e., 5-anode) and cathode (i.e., 90 s-Pt-sputtered CF) in the PBS solutions containing 10 and 300 mmol L $^{-1}$ glucose under ambient conditions. Furthermore, these BFC electrodes were fabricated using single, two-ply, and three-ply electrodes for both anode and cathode. During the fabrication process of the multi-ply fiber electrode, the largest and smallest diameter parts were repeated to create a multi-ply fiber electrode. In this case, the total active surface area was calculated using the value of the largest diameter of the multi-ply fiber electrode. However, due to the overlapping of several fiber electrodes to form one BFC electrode, the active surface area provided was larger than the overall increase in the diameter of the multi-ply fiber electrode. This phenomenon suggests that a multi-ply fiber-based BFC can generate a higher areal power density (Figure 5a and Figure S36, Supporting Information).

To exclude the parasitic currents at the anode and cathode, stationary power outputs were measured by the external circuit resistance method. First, the power density of BFCs with the Pt-sputtered cathode was ≈ 1.36 times higher than that of BFCs with the Pt-free cathode (Figure S37, Supporting Information). Specifically, when measuring the power outputs of three different kinds of BFCs with (OAm-ITO NP/GOx)_{p=1, 3, and 5} multilayers using the external circuit resistance method, their power outputs in 300 mmol L $^{-1}$ glucose under ambient conditions were 2.1, 3.1, and 4.7 mW cm $^{-2}$, respectively (Figure 5b and Figure S38, Supporting Information). When using a low glucose concentration of 10 mmol L $^{-1}$ (corresponding to physiological conditions), these BFCs exhibited power densities of ≈ 1.4 (for $p = 1$), 1.7 (for $p = 3$), and 2.0 mW cm $^{-2}$ (for $p = 5$) with an OCV of ≈ 0.83 V, respectively (Figure 5c and Figure S39, Supporting Information). Although the use of low glucose concentration resulted in a relatively low power output of the BFCs, it is important to highlight that our CF-based BFC produced significantly higher power output compared to previously reported BFCs with excellent performance, achieving ≈ 2.0 mW cm $^{-2}$ under 10 mmol L $^{-1}$ glucose (See Table S1, Supporting Information).

Another notable feature is that the areal power output of BFC can be significantly enhanced through the simple multi-ply structure of fiber anodes. Specifically, with increasing the ply number up to 3, the power density of multi-ply BFCs (in 300 mmol L $^{-1}$ glucose under ambient conditions) increased up to 10.4 mW cm $^{-2}$ with an OCV of ≈ 1 V, which outperformed the power outputs of BFCs reported to date (Figure 5d,e, Figures S40 and S41, and Table S1, Supporting Information). Furthermore, the three-ply BFC exhibited high operational stability, maintaining $\approx 49\%$ (2.2 mW cm $^{-2}$) of its initial power density after continuous operations for 60 days in 10 mmol L $^{-1}$ glucose

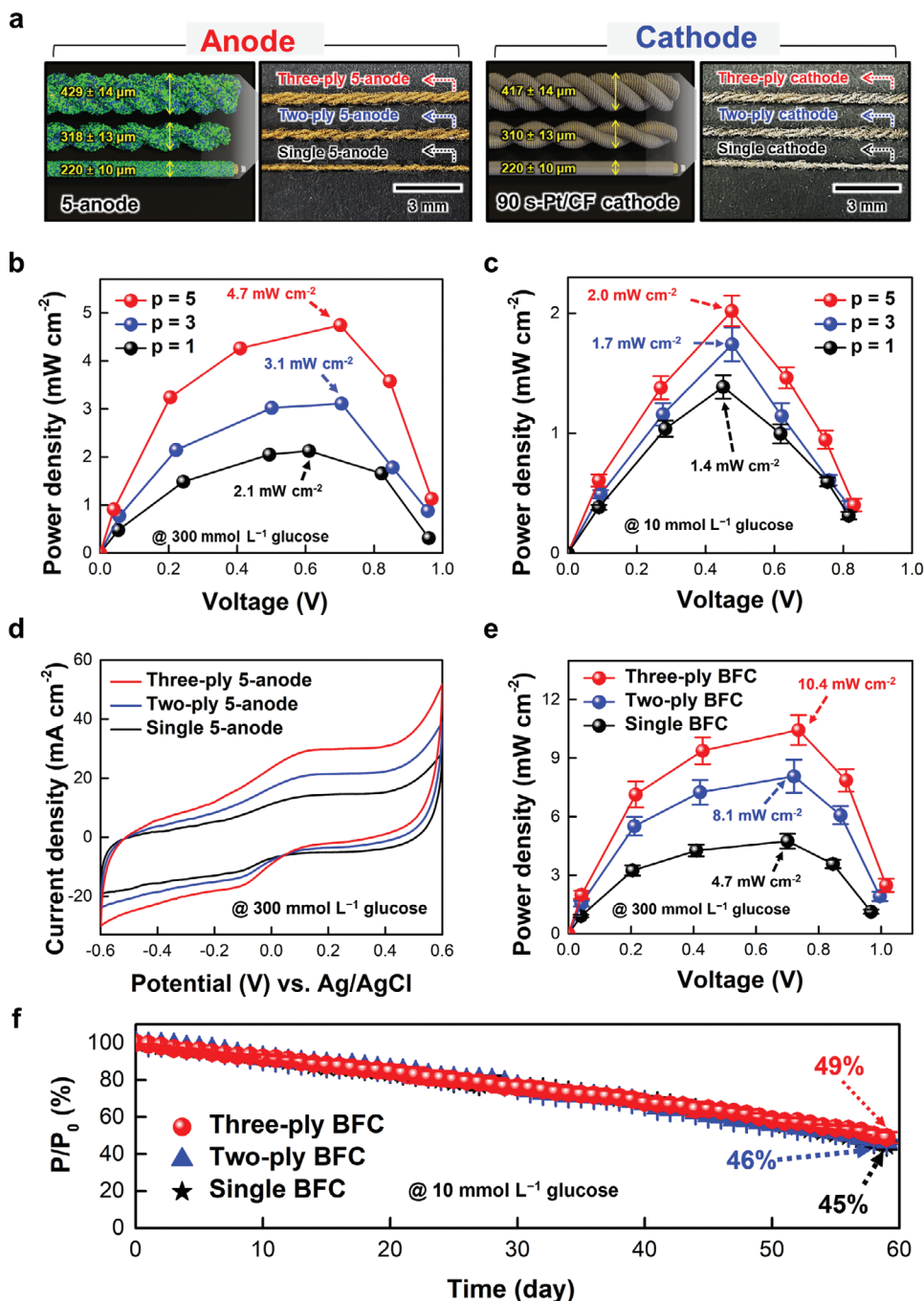


Figure 5. Performance of complete BFCs of multi-ply electrodes. a) Schematic illustration and photographic images of multi-ply anode and cathode. b) Power output of the complete BFCs as a function of bilayers number (p) in PBS solution containing 300 mmol L⁻¹ glucose at 36.5 °C. c) Power output of the complete BFCs as a function of bilayers number (p) in PBS solution containing 10 mmol L⁻¹ glucose at 36.5 °C. d) CV curves of the multi-ply structured 5-anode. e) Power output of the complete BFCs of multi-ply electrodes in PBS solution containing 300 mmol L⁻¹ glucose at 36.5 °C. f) Relative power retention (P/P_0) of the complete BFCs of multi-ply electrodes in PBS solution containing 10 mmol L⁻¹ glucose at 36.5 °C.

(maintaining $\approx 60\%$ (≈ 6.2 mW cm⁻²) of its initial power density after 20 days in 300 mmol L⁻¹ glucose) (Figure 5f and Figure S42, Supporting Information). In the case of single- and two-ply BFCs, they maintained $\approx 45\%$ (≈ 0.9 mW cm⁻²) and 46% (≈ 1.6 mW cm⁻²) of their initial power density even after 60 days. It should be noted that this high operational stability is caused by

multiple affinities between GOx and OAm-ITO NPs as well as between CF and GOx. Particularly, considering that an excessive increase in the loading amount of GOx in the anode has an adverse effect on the anodic performance, our approach using multi-ply electrodes can provide a promising tool for developing BFCs with high-power output and long-term stability. However, given that

our BFC electrodes incorporate various components, including ITO NPs, COOH-MWCNTs, Au NPs, and Pt, it is essential and desirable to conduct comprehensive investigations into their biological toxicity before considering their use in implantable BFC-based devices.

3. Conclusion

In this study, we have successfully demonstrated the significant improvements achieved in electron transfer efficiency and operational stability of mediator-free BFCs through the nanoblended OAm-ITO NP/GOx multilayers on the host CF electrode. By leveraging interfacial interactions and electron transfer at the GOx/CF and GOx/GOx interfaces, we have observed enhanced performance in our BFCs. The incorporation of OAm-ITO NPs with distinctive shapes, despite their hydrophobic properties, has further contributed to the success of our hybrid BFCs by forming a perfect nanoblended GOx/OAm-ITO NP film and creating efficient electron pathways within the anode. The utilization of a multi-ply high-performance fiber electrode has also played a crucial role in our achievements. The highly porous structure and large active surface area of the multi-ply electrodes have substantially increased the areal power density without compromising ion transfer kinetics. Additionally, the incorporation of organic linkers, such as TREN, with extremely low M_w has facilitated the increase in electrical conductivity of the host CF electrode through hydrogen bonding between neighboring COOH-MWCNTs.

Based on the various benefits of our approach, including the fiber-type host electrode, the conductive OAm-ITO NP-incorporated anodes, the Pt-sputtered cathodes, and the multi-ply electrode system, we have achieved remarkable results. Our three-ply CF-based BFC has exhibited an exceptional areal power density of $\approx 10.4 \text{ mW cm}^{-2}$, surpassing previously reported BFCs. Furthermore, even at a glucose concentration close to physiological conditions (10 mmol L^{-1}), our three-ply BFCs have maintained $\approx 49\%$ of the initial power density over a continuous operation of 60 days. These findings highlight the effectiveness and uniqueness of conductive oxide NP-incorporated enzyme deposition and multi-ply approaches in enhancing the energy performance of various bio-electrochemical energy devices and BFCs.

4. Experimental Section

Detailed experimental information is available in part of the Supporting Information.

Supporting Information

Supporting Information is available from the Wiley Online Library or from the author.

Acknowledgements

M.K., D.Y., and J.A. contributed equally to this work. This work was supported by the National Research Foundation of Korea (NRF) grant funded by the Korean Government (Ministry of Science and ICT) (NRF-2021R1A2C3004151, 2022R1A2C1009690) and the KU-KIST School Program.

Conflict of Interest

The authors declare no conflict of interest.

Data Availability Statement

The data that support the findings of this study are available from the corresponding author upon reasonable request.

Keywords

a mediator-free biofuel cell, a multi-ply electrode, conductive oxide nanoparticles, enzymes

Received: May 26, 2023

Revised: August 18, 2023

Published online:

- [1] X. Xiao, H. Xia, R. Wu, L. Bai, L. Yan, E. Magner, S. Cosnier, E. Lojou, Z. Zhu, A. Liu, *Chem. Rev.* **2019**, *119*, 9509.
- [2] A. J. Bandodkar, *J. Electrochem. Soc.* **2017**, *164*, H3007.
- [3] S. Cosnier, A. Le Goff, M. Holzinger, *Electrochem. Commun.* **2014**, *38*, 19.
- [4] A. Zebda, J. P. Alcaraz, P. Vadgama, S. Shleev, S. D. Minteer, F. Boucher, P. Cinquin, D. K. Martin, *Bioelectrochemistry* **2018**, *124*, 57.
- [5] A. T. Yahiro, S. M. Lee, D. O. Kimble, *Biochim. Biophys. Acta.* **1964**, *88*, 375.
- [6] A. Heller, *Phys. Chem. Chem. Phys.* **2004**, *6*, 209.
- [7] S. C. Barton, J. Gallaway, P. Atanassov, *Chem. Rev.* **2004**, *104*, 4867.
- [8] R. A. Bullen, T. C. Arnot, J. B. Lakeman, F. C. Walsh, *Biosens. Bioelectron.* **2006**, *21*, 2015.
- [9] C. H. Kwon, M. Kang, M. Kwon, D. Nam, Y. Song, E. Yong, M.-K. Oh, Y. Kim, B. Yeom, J. H. Moon, S. W. Lee, J. Cho, *Appl. Phys. Rev.* **2022**, *9*, 021413.
- [10] F. Davis, S. P. Higson, *Biosens. Bioelectron.* **2007**, *22*, 1224.
- [11] C. H. Kwon, Y. Ko, D. Shin, M. Kwon, S. W. Lee, J. Cho, *J. Mater. Chem. A* **2019**, *7*, 13495.
- [12] S. D. Minteer, B. Y. Liaw, M. J. Cooney, *Curr. Opin. Biotechnol.* **2007**, *18*, 228.
- [13] I. Willner, Y. M. Yan, B. Willner, R. Tel-Vered, *Fuel Cells* **2009**, *9*, 7.
- [14] M. J. Cooney, V. Svoboda, C. Lau, G. Martin, S. D. Minteer, *Energy Environ. Sci.* **2008**, *1*, 320.
- [15] A. A. Babadi, W. A. A. Q. I. Wan, J.-S. Chang, Z. Ilahm, A. A. Jamaludin, G. Zamiri, O. Akbarzadeh, W. J. Basirun, *Int. J. Hydrog. Energy* **2019**, *44*, 30367.
- [16] B. Reuillard, A. Le Goff, C. Agnes, M. Holzinger, A. Zebda, C. Gondran, S. Cosnier, *Phys. Chem. Chem. Phys.* **2013**, *15*, 4892.
- [17] Z. Zhong, L. Qian, Y. Ran, G. Wang, L. Yang, C. Hou, A. Liu, *J. Electroanal. Chem.* **2018**, *823*, 723.
- [18] A. Ruff, F. Conzuelo, W. Schuhmann, *Nat. Catal.* **2020**, *3*, 214.
- [19] J. W. Gallaway, S. A. Calabrese Barton, *J. Am. Chem. Soc.* **2008**, *130*, 8527.
- [20] A. Heller, *J. Phys. Chem.* **1992**, *96*, 3579.
- [21] Y. Degani, A. Heller, *J. Am. Chem. Soc.* **1989**, *111*, 2357.
- [22] W. Schuhmann, T. J. Ohara, H. L. Schmid, A. Heller, *J. Am. Chem. Soc.* **1991**, *113*, 1394.
- [23] P. N. Bartlett, V. Q. Bradford, R. G. Whitaker, *Talanta* **1991**, *38*, 57.
- [24] A. Niiyama, K. Murata, Y. Shigemori, A. Zebda, S. Tsujimura, *J. Power Sources* **2019**, *427*, 49.
- [25] H. Sakai, T. Nakagawa, Y. Tokita, T. Hatazawa, T. Ikeda, S. Tsujimura, K. Kano, *Energy Environ. Sci.* **2009**, *2*, 133.

- [26] X. Xiao, H. Xia, R. Wu, L. Bai, L. Yan, E. Magner, S. Cosnier, E. Lojou, Z. Zhy, A. Liu, *Chem. Rev.* **2019**, *119*, 9509.
- [27] M. Cadet, S. Gounel, C. Stines-Chaumeil, X. Brilland, J. Rouhana, F. Louerat, N. Mano, *Biosens. Bioelectron.* **2016**, *83*, 60.
- [28] S. H. Rijt, P. J. Sadler, *Drug Discovery Today* **2009**, *14*, 1089.
- [29] L. Hussein, G. Urban, M. Krüger, *Phys. Chem. Chem. Phys.* **2011**, *13*, 5831.
- [30] M. H. Kabir, E. Marquez, G. Djokoto, M. Parker, T. Weinstein, W. Ghann, J. Uddin, M. M. Ali, M. M. Alam, M. Thompson, A. S. Poyraz, H. Z. Msimanga, M. M. Rahman, M. Rulison, J. Cramer, *ACS Appl. Mater. Interfaces* **2022**, *14*, 24229.
- [31] P. Gai, R. Song, C. Zhu, Y. Ji, Y. Chen, J. R. Zhang, J. J. Zhu, *Chem. Commun.* **2015**, *51*, 14735.
- [32] J. M. Abad, M. Gass, A. Bleloch, D. J. Schiffrin, *J. Am. Chem. Soc.* **2009**, *131*, 10229.
- [33] C. Gutierrez-Sanchez, M. Pita, C. Vaz-Dominguez, S. Shleev, A. L. De Lacey, *J. Am. Chem. Soc.* **2012**, *134*, 17212.
- [34] J. T. Holland, C. Lau, S. Brozik, P. Atanassov, S. Banta, *J. Am. Chem. Soc.* **2011**, *133*, 19262.
- [35] K. Murata, K. Kajiya, N. Nakamura, H. Ohno, *Energy Environ. Sci.* **2009**, *2*, 1280.
- [36] N.-B. Noh, Y. B. Shim, *J. Mater. Chem. A* **2016**, *4*, 2720.
- [37] T. Nöll, G. Nöll, *Chem. Soc. Rev.* **2011**, *40*, 3564.
- [38] M. Zayats, E. Katz, I. Willner, *J. Am. Chem. Soc.* **2002**, *124*, 2120.
- [39] Y. Xiao, F. Patolsky, E. Katz, J. F. Hainfeld, I. Willner, *Science* **2003**, *299*, 1877.
- [40] S. A. Ansari, Q. Husain, *Biotechnol. Adv.* **2012**, *30*, 512.
- [41] A. Zebda, C. Gondran, A. Le Goff, M. Holzinger, P. Cinquin, S. Cosnier, *Nat. Commun.* **2011**, *2*, 370.
- [42] J. J. Virgen-Ortiz, J. C. Dos Santos, A. Berenguer-Murcia, O. Barbosa, R. C. Rodrigues, R. Fernandez-Lafuente, *J. Mat. Chem. B* **2017**, *5*, 7461.
- [43] Y. Chung, K. H. Hyun, Y. Kwon, *Nanoscale* **2016**, *8*, 1161.
- [44] Y. Lvov, K. Ariga, I. Ichinose, T. Kunitake, *J. Am. Chem. Soc.* **1995**, *117*, 6117.
- [45] L. L. Coria-Oriundo, M. L. Cortez, O. Azzaroni, F. Battaglini, *Soft Matter* **2021**, *17*, 5240.
- [46] K. H. Hyun, S. W. Han, W.-G. Koh, Y. Kwon, *J. Power Sources* **2015**, *286*, 197.
- [47] F. Mao, N. Mano, A. Heller, *J. Am. Chem. Soc.* **2003**, *125*, 4951.
- [48] H. J. Sim, D. Y. Lee, H. Kim, Y.-B. Choi, H.-H. Kim, R. H. Baughman, S. J. Kim, *Nano Lett.* **2018**, *18*, 5272.
- [49] M. N. Zafar, I. Aslam, R. Ludwig, G. Xu, L. Gorton, *Electrochim. Acta* **2019**, *295*, 316.
- [50] C. Peng, Y. S. Thio, R. A. Gerhardt, *J. Phys. Chem. C* **2010**, *114*, 9685.
- [51] Y. Kim, J. Zhu, B. Yeom, M. D. Prima, X. Su, J.-G. Kim, S. J. Yoo, C. Uher, N. A. Kotov, *Nature* **2013**, *500*, 59.
- [52] S. Roy, A. N. M. W. Azad, S. Baidya, M. K. Alam, F. Khan, *IEEE Trans. Power Electron.* **2022**, *37*, 12237.
- [53] Y. Shao, M. F. El-Kady, J. Sun, Y. Li, Q. Zhang, M. Zhu, H. Wang, B. Dunn, R. B. Kaner, *Chem. Rev.* **2018**, *118*, 9233.
- [54] U. P. Do, F. Seland, K. Wang, E. A. Johannessen, *J. Mater. Sci.* **2019**, *54*, 14143.
- [55] M. Q. Hasan, R. Kuis, J. S. Narayanan, G. Slaughter, *Sci. Rep.* **2018**, *8*, 16351.
- [56] Y. Oztekin, A. Ramanaviciene, A. Yazicigil, A. O. Solac, A. Ramanavicius, *Biosens. Bioelectron.* **2011**, *26*, 2541.
- [57] E. Laviron, *J. Electroanal. Chem.* **1979**, *101*, 19.
- [58] X. Kang, J. Wang, H. Wu, I. A. Aksay, J. Liu, Y. Lin, *Biosens. Bioelectron.* **2009**, *25*, 901.
- [59] C. Cai, J. Chen, *Anal. Biochem.* **2004**, *332*, 75.
- [60] S. ul Haque, A. Nasar, A. M. Asiri, *Chem. Phys. Lett.* **2018**, *692*, 277.
- [61] H. J. Hecht, H. M. Kalisz, J. Hendle, R. D. Schmid, D. Schomburg, *J. Mol. Biol.* **1993**, *229*, 153.
- [62] G. J. Brug, A. L. van den Eeden, M. Sluyters-Rehbach, J. H. Sluyters, *J. Electroanal. Chem.* **1984**, *176*, 275.
- [63] Z. Yin, Z. Ji, W. Zhang, E. W. Taylor, X. Zeng, J. Wei, *ChemistrySelect* **2020**, *5*, 12224.
- [64] Y.-M. Yan, I. Baravik, O. Yehezkeli, I. Willner, *J. Phys. Chem.* **2008**, *112*, 17883.